ACS APPLIED MATERIALS & INTERFACES
Research Article
www.acsami.org

Designing Theranostic Agents Based on Pluronic Stabilized Gold Nanoaggregates Loaded with Methylene Blue for Multimodal Cell Imaging and Enhanced Photodynamic Therapy

Timea Simon,[†] Monica Potara,[†] Ana-Maria Gabudean,[†] Emilia Licarete,[‡] Manuela Banciu,[‡] and Simion Astilean*[,†]

[†]Nanobiophotonics and Laser Microspectroscopy Center, Interdisciplinary Research Institute in Bio-Nano-Sciences and Faculty of Physics, and [‡]Molecular Biology Center, Interdisciplinary Research Institute in Bio-Nano-Sciences and Faculty of Biology, Babes-Bolyai University, M. Kogalniceanu Str 1, 400084 Cluj-Napoca, Romania

Ⓢ *Supporting Information*

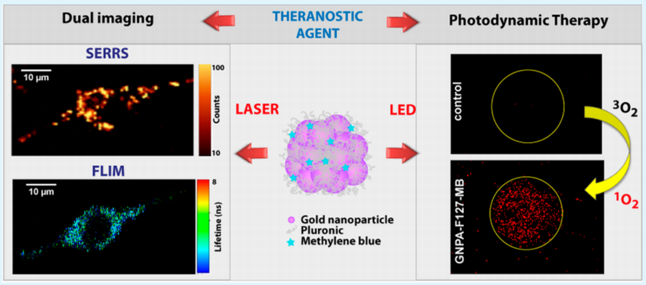

ABSTRACT: At present, multifunctional noble metal-based nanocomposites are extensively investigated for their potential in performing cellular imaging, diagnostics, and therapy by integration of unique plasmonic properties with the spectroscopic expression and therapeutic activity of appropriate drug. In this work, we report the fabrication of 3-dimensional (3-D) close-packed nanoassemblies of gold nanoparticles by controlling the aggregation of individual nanoparticles in solution and subsequent stabilization of formed aggregates by Pluronic block copolymer (F127) coating. Besides conferring high stability, Pluronic mediates the loading of Methylene Blue (MB) molecules which exhibit interesting spectroscopic and photochemical properties to be employed as both optical label and photosensitizing drug. Indeed, here we demonstrate the pertinence of the fabricated nanoassemblies to provide optical imaging of murine colon carcinoma cells (C-26) via both Raman and fluorescence signals collected from MB molecules, specifically by using scanning confocal surface-enhanced resonant raman spectroscopy (SERRS) and fluorescence lifetime imaging microscopy (FLIM) techniques. The specific configuration of as fabricated nanoassemblies allows a small population of MB molecules to be located in very small areas between the aggregated nanoparticles ("hot spots") to provide SERRS signal while the other population remains captured in Pluronic coating and preserves both its fluorescence signal and singlet-oxygen generation capability. Remarkably, we demonstrate an enhanced photodynamic therapeutic activity of MB-loaded gold nanoaggregates against murine colon carcinoma cells (C-26), as compared to the free photosensitizer. To our knowledge, this is the first report on plasmonic nanoplatforms conveying photosensitizing drug into cells to operate as optical label via both SER(R)S and FLIM and to perform enhanced photodynamic therapy.

KEYWORDS: *gold, nanoaggregates, methylene blue, SERS, FLIM, PDT*

1. INTRODUCTION

Notwithstanding the progression and benefits that nanotechnology has provided to medicine, numerous challenges still persist. Early diagnosis of the disease, efficient targeting of the affected sites, and real-time in vivo monitoring of the drug delivery and of the efficiency of treatments and therapies are far from being considered as resolved issues. Successful attempts have been carried out to develop more specific, personalized therapies for various diseases, especially for cancer, and to combine them with diagnostic tools in order to precisely localize the affected sites and monitor the targeted treatments.[1−3] A new term *theranostics* was recently introduced to denote this promising combination of diagnostic and therapy. In this context, the design of multifunctional nanoparticles able to carry both diagnostic and therapeutic probes has become one of the main research topics in the biomedical field. Among the various types of nanoplatforms that have been extensively investigated for cancer theranostics, gold nanoparticles proved to be one of the most appealing candidates due to their biocompatibility, tunable optical properties, easy fabrication methods, and the diverse possibilities of surface functionalization.[4] Due to their strong interaction with light, gold nanoparticles have been widely exploited as building up materials of both imaging and therapeutic agents.[5−7] The enhanced electromagnetic field around the gold nanoparticles as a result of surface plasmon excitation is known to have considerable effects on the spectroscopic response of organic molecules located in their closed vicinity, giving rise to a number of remarkable effects with particular interest in imaging and detection applications, such as surface enhanced raman

Received: November 4, 2014
Accepted: July 7, 2015
Published: July 7, 2015

DOI: 10.1021/acsami.5b04734
ACS Appl. Mater. Interfaces 2015, 7, 16191−16201

scattering (SERS)[8] or metal-enhanced fluorescence (MEF).[9] Furthermore, not only could the intrinsic radiative processes benefit from the vicinity of gold nanoparticles but the therapeutic activity of drug molecules can also be improved. For instance, it has been repeatedly demonstrated that the photodynamic activity of photosensitizers in the presence of plasmonic nanoparticles increases significantly.[10−12] The observed metal-enhanced singlet oxygen generation (MESOG) can be attributed to the enhanced excitation rate due to the metal and the subsequent enhancement of intersystem crossing and excited state triplet yield. Furthermore, if photosensitizers are conjugated to nanoparticles with plasmon resonance band in the biological window of the tissue, the light-to-heat conversion effect can be also exploited in order to perform combined anticancer therapy via dual plasmon-assisted hyperthermia and photodynamic therapy (PDT).[13] Piecing together all the components in view of the best imaging and therapeutic performance is not the only challenge when constructing a theranostic agent. Biocompatibility and good stability in biological media is another requirement to be fulfilled, and it is certainly a delicate issue. The application of a protective coating, such as (bio)polymers or silica, is a frequently used approach to stabilize nanoparticles, endowing biocompatibility and enabling further biofunctionalization with targeting moieties.[14] Apart from the above-mentioned properties, the polymer layer can be further exploited to modulate the distance between nanoparticles and imaging or therapeutic agents in order to optimize their efficiency.

In this work we present the fabrication and the pertinence of a new class of multifunctional nanotags carrying both imaging and therapeutic potentials. The design of this theranostic agent is based on small gold nanoparticle aggregates stabilized with Pluronic F127 block copolymer (GNPA-F127). The well-known photosensitizing drug, Methylene Blue (MB), was loaded into GNPA-F127, which also serves as both Raman reporter and fluorescence label. The SERRS enhancement is achieved through the cooperation of two mechanisms, specifically the highly amplified electromagnetic field in so-called "hot spots" of aggregated nanoparticles and the electronic resonant excitation of MB, resulting in a drastic amplification of the Raman signal of molecules trapped in the junction between nanoparticles.[15] Besides its role in stabilization and biocompatibilization, Pluronic acts also as a spacer against fluorescence quenching for distinct population MB molecules, allowing in this way fluorescent detection of the nanoparticles. Furthermore, the encapsulation of MB in the Pluronic shell of GNPA-F127 within enhanced plasmonic field increases both the fluorescence lifetime and the excitation rate, which all together have positive impact on the intersystem crossing rate and singlet oxygen generation efficiency.

As the accurate localization of the nanoparticles inside cells and evincing the possible interaction with cellular components is crucial in view of an effective diagnosis and therapy, we first focus on the investigation of the cellular imaging ability of MB-loaded GNPA-F127 (GNPA-F127-MB) via scanning surface enhanced raman spectroscopy (SERS) and fluorescence lifetime imaging (FLIM). Furthermore, we evaluate the in vitro PDT performance of the GNPA-F127-MB against murine colon carcinoma cancer cells (C-26) and demonstrate that GNPA-F127-MB are photoactivated under LED irradiation at 660 nm wavelength and provide improved PDT efficiency relative to free photosensitizer drug. Finally, we show that our nanoparticles satisfy the criteria of low dark cytotoxicity, which is imperative for any future development of real biomedical applications.

2. EXPERIMENTAL SECTION

2.1. Chemicals. Hydrogen tetrachloroaurate(III) trihydrate ($HAuCl_4 \cdot 3H_2O$), trisodium citrate, sodium chloride (NaCl), Pluronic F127, Methylene Blue (MB), and Propidium Iodide solution (1.0 mg/mL in water) (PI) were purchased from Sigma-Aldrich. 1,3-Diphenylisobenzofuran (DPBF) was obtained from Alfa Aesar. All chemicals were used without further purification. Ultrapure water was used as solvent throughout the experiments.

2.2. Synthesis and Stabilization of Gold Nanospheres (GNP-F127). Citrate-capped spherical gold nanoparticles (GNP) were synthesized by the aqueous reduction of $HAuCl_4$ with trisodium citrate according to the Turkevich−Frens method.[16] Briefly, 100 mL of 10^{-3} M $HAuCl_4 \cdot 3H_2O$ was boiled, and a solution of 38.8×10^{-3} M sodium citrate (10 mL) was quickly added under vigorous stirring. During the boiling process the solution changed its color from yellow to intense burgundy-red. Then, the solution was removed from the heat, and the stirring process continued for another 10−15 min. Stabilization of the GNP was realized by their coincubation using Pluronic F127 at a final concentration of 4×10^{-4} M. The Pluronic encapsulated GNP (GNP-F127) colloidal solution was purified from the unbound polymer chains by centrifugation at 12 000 rpm for 20 min.

2.3. Formation and Stabilization of the Gold Nanoparticle Aggregates (GNPA-F127). The pristine colloidal solution of citrate-capped gold nanoparticles was purified from unbound molecules by centrifugation at 12 000 rpm for 10 min. Afterward, to 1 mL of purified colloid 500 μL of methanol was added followed by the rapid injection of 15 μL of NaCl 1 M. An immediate color change from deep red to purple was observed upon mixing the solutions, indicating the aggregation of nanoparticles. The formed aggregates were stabilized with 4×10^{-4} M Pluronic F127 (GNPA-F127) and purified by centrifugation at 10 000 rpm for 10 min.

2.4. Gold Nanoparticles Loading with Methylene Blue (GNP-F127-MB, GNPA-F127-MB). Both GNP-F127 and GNPA-F127 colloidal solutions were mixed with an aqueous MB solution at a final concentration of 2×10^{-5} M and incubated at room temperature for 2 h. The colloidal solutions were purified from any MB molecules by centrifugation for 10 min at 10 000 rpm. The concentration of MB loaded was calculated according to the Beer−Lambert law, by subtracting the amount of MB measured in supernatant from the amount of MB measured in initially prepared solution. GNPA-F127-MB have a final MB concentration of 1.7×10^{-6} M, while in the case of GNP-F127-MB the final MB concentration is 4×10^{-6} M.

2.5. Detection of the Singlet Oxygen Generation. The 1,3-diphenylisobenzofuran (DPBF) was used as indirect chemical probe to characterize the release of singlet oxygen into the solution by as-prepared nanoparticles (GNP-F127-MB, GNPA-F127-MB) under irradiation in ethanol. The reaction of chemical oxidation was monitored by recording the decrease in absorption of DPBF at 410 nm via UV−vis absorption spectroscopy. GNPA-F127-MB, GNPA-F127, and MB solutions (concentration of 1.7×10^{-6} M) were mixed with the DPBF solution in final concentration of 8×10^{-5} M. The samples were irradiated in a quartz cuvette at 660 nm wavelength light coming from a LED (Thorlabs), and the absorption intensity of DPBF at 410 nm was monitored as a function of time up to 150 s of irradiation. Control measurements were carried out in the same experimental conditions on pure ethanolic solution of DPBF of 8×10^{-5} M.

2.6. Cell Culture and Incubation Conditions. Murine colon carcinoma cells (C-26, Cell Line Service, Germany) were grown in RPMI culture medium (Lonza), supplemented with 2 mM L-glutamine, penicillin/streptomycin 100 U/mL, 10% fetal calf serum and incubated in a humidified incubator (37 °C, 5% CO_2). For time-resolved fluorescence, dark field (DF), differential interference contrast (DIC) imaging, and PDT assays 3×10^4 cells were grown on Ibidi 30 μ-Dish (50 mm). For Raman measurements, cells were seeded on 24 × 50 mm cover glass. After 24 h of cultivation, the culture medium was replaced with complete culture medium containing GNPA-F127-MB/

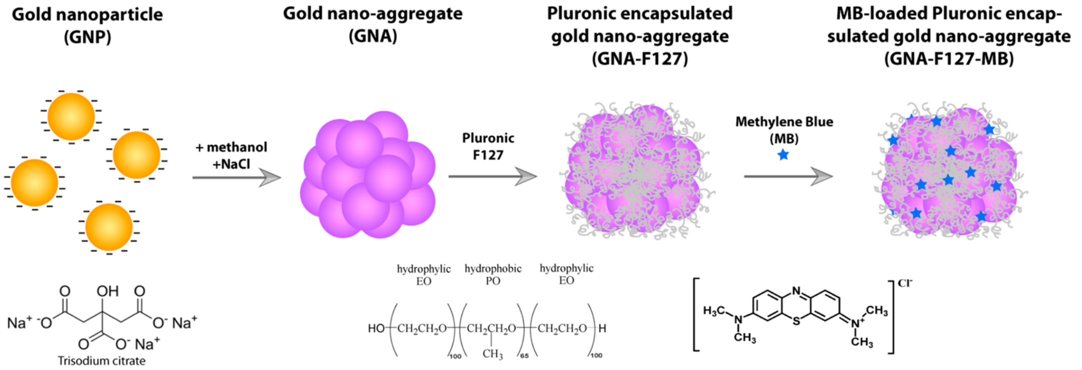

Figure 1. Schematic illustration of the preparation process of GNPA-F127-MB.

GNPA-F127 nanoparticles (40 μg/mL) and incubated for another 24 h. Prior to imaging assays, cells were rinsed three times with phosphate-buffered saline (PBS) and fixed with 5% paraformaldehyde.

2.7. Cytotoxicity Assay. The cytotoxic effect of nanoparticles (GNPA-F127-MB and GNPA-F127) was assayed using WST-1 dye (water-soluble tetrazolim salt, Millipore) assay based on the enzymatic cleavage of the tetrazolium salt WST-1 to formazan by mitochondrial dehydrogenases active in the living cells. Therefore, 1×10^4 cells/well were cultured in a 96-well plate. After 24 h, the culture medium was removed, and fresh medium containing between 20/120 μg/mL GNPA-F127-MB/GNPA-F127 was added to the test wells, and the cells were placed in the incubator for an additional 24 h. Each concentration was tested in triplicate. Cells without nanoparticles were used as positive control. At the end of the incubation period, medium was removed from all wells, and 100 μL of fresh medium containing 10% WST-1 solution was added to each well. Empty wells with medium containing WST-1 reagent were used as blank. After 60 min of incubation, the absorbance was measured at 440 nm, using a microplate reader (FlostarOmega, BMG, Germany). A reference wavelength was used at 650 nm.

2.8. Experimental Measurements. Extinction spectra were recorded using a Jasco V-670 UV−vis−NIR spectrometer with a slit width of 2 and 1 nm spectral resolution. The morphology of the gold nanoparticles was examined using a JEOL 100 U type transmission electron microscope operated at 100 kV accelerating voltage. Zeta potential was measured by a Zetasizer NanoZS90 instrument (Malvern Instruments) at 20 °C.

DF and DIC microscopy of C-26 cells incubated with nanoparticles was performed on an inverted Zeiss Axio Observer Z1 microscope. A 100 W halogen lamp was used for DF illumination which was focused on the sample using a high numerical immersion DF condenser (NA = 1.4), and the scattered light was collected by an A-Plan 100× objective (NA = 0.8, Zeiss). DIC imaging was performed using a long distance condenser (NA = 0.8) with specific DIC prisms for illumination, and collection was performed with a Plan-Apochromat/DIC 100× oil immersion objective (NA = 1.4, Zeiss). Images were acquired using an AxioCam Icc digital camera and processed by the ZEN software.

Raman and SERRS measurements were performed on a Confocal Raman Microscope (alpha 300R from WITec GmbH, Germany). The cells grown on glass slides were inserted in a 60 mm Petri dish filled with PBS and mounted on a piezolelectric scanning stage. A 532 nm excitation line from a Nd:YAG laser was used for Raman imaging, while SERRS imaging of cells was obtained using a 633 nm line from a He−Ne laser. A W-plan Apochromat 63× water immersion objective (NA = 1, WD = 2.1 mm, Zeiss) was used to perform all spectroscopic measurements from cells. The Raman backscattered light collected through the objective was passed through a holographic edge filter, before being focused into a multimode optical fiber of 100 μm diameter which provides the optical pinhole for confocal measurement. The light emerging from the output optical fiber was analyzed by ultrahigh throughput spectrometer equipped with back-illuminated deep-depletion 1024 × 128 pixel CCD camera operating at −60 °C (DV401-BV, Andor). For optical sectioning measurements of cells, five sections were scanned using 2 μm optical slices in the Z-direction. The spectroscopic cell imaging was performed over a 30 × 60 μm^2 area by choosing an integration time of 0.1 s and laser power of 1.1 mW for each spectrum in the case of SERRS imaging using 633 nm excitation laser line and 0.3 s and 14 mW power in the case of Raman imaging at 532 nm. With the above parameters, SERRS imaging took about 10 min/image and Raman imaging 30 min/image. SERRS and Raman maps were obtained by integrating the intensity of the 1623 cm^{-1} band of MB and C−H stretching vibrations band of lipids at 2800−3100 cm^{-1}, respectively.

The reference SER(R)S spectra were recorded directly from the GNPA-F127-MB and GNP-F127-MB colloidal solutions through a 20× objective (NA = 0.4), employing for excitation the 633 and 532 nm wavelength (∼5 mW power on sample). The integration time was set at 10 s per spectrum. The WITec Project Four Plus software was used for spectral analysis and image processing.

Fluorescence lifetime measurements were performed on a PicoQuant MicroTime 200 time-resolved confocal fluorescence microscope system based on an inverted microscope (IX 71, Olympus) equipped with a UPLSAPO 60× water immersion objective (NA = 1.2). The excitation beam was provided by a 0.55 μW picosecond diode laser head (LDH-D-C-640, PicoQuant) operating at 640 nm and 40 MHz repetition rate. The samples were dropped on microscope cover glasses and analyzed in solution. The signal collected through the objective was spatially and spectrally filtered by a 50 μm pinhole and a HQ690/70 (Chroma, Brattleboro, U.S.A.) emission filter, respectively, before being focused on a photon counting detector module (PDM) Single Photon Avalanche Diode (SPAD) from (Micro Photon Devices) MPD. The detector signals were processed by the PicoHarp 300 Time-Correlated Single Photon Counting (TCSPC) data acquisition unit, from PicoQuant. Data were recorded and analyzed using the SymPhoTime software from PicoQuant. Experimental fluorescence decay curves were tail-fitted with exponential decay curves, while the quality of the fits was judged by analyzing the chi-square (χ^2) values and the distribution of the residuals.

2.9. PDT Assay. For PDT assays, C-26 cells were seeded on an Ibidi 30 μ-Dish (50 mm) and incubated for 24 h with GNPA-F127-MB/GNPA-F127 nanoparticles at a final nanoparticle concentration of 40 μg/mL and with free MB at an equivalent concentration of 1.7×10^{-6} M. After incubation, the cells were rinsed with 1% PBS to remove the uninternalized nanoparticles/molecules and replaced with fresh cell culture medium. PDT assays were performed on an inverted Zeiss Axio Observer Z1 microscope equipped with incubator to maintain the optimum conditions for cells (37 °C, 5% CO_2). A spot of 600 μm in diameter was irradiated by focusing the light coming from a 660 nm LED (Thorlabs, equipped with a collimator and a LED driver to control the intensity) through a 40× objective (Zeiss, EC Plan-Neofluar, NA = 1.3). Evaluation of cell death in the irradiated zones was performed 3 h after irradiation in transmitted light and fluorescence mode by staining with propidium iodide (PI). A HXP 120 lamp was used for fluorescence excitation, and all the images were collected by a 10× objective (Zeiss, Plan-Apochromat, NA = 0.45).

DOI: 10.1021/acsami.5b04734
ACS Appl. Mater. Interfaces 2015, 7, 16191−16201

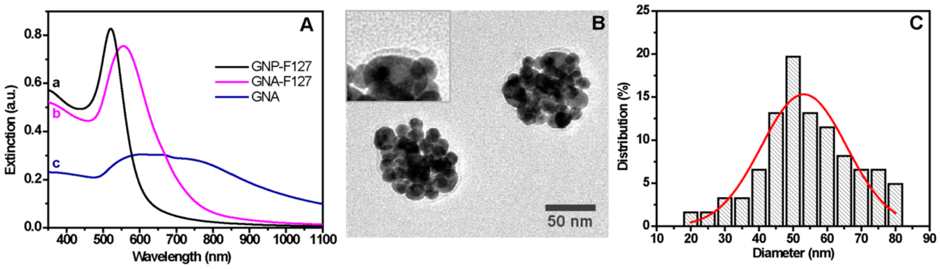

Figure 2. (A) Extinction spectra of colloidal solutions of GNP-F127 (a), GNPA-F127 (b), and GNPA without encapsulation in Pluronic; (B) representative TEM picture of GNPA-F127 showing the Pluronic coating (see zoomed inset). (C) Size distribution histogram of GNPA-F127 fitted with a Gaussian curve.

3. RESULTS AND DISCUSSION

3.1. Preparation and Characterization of MB-Loaded Gold Nanoaggregates.

UV–Vis–NIR Characterization. Controlled aggregation of individual GNPs, their polymer stabilization, and MB drug loading are schematically illustrated in Figure 1. First, the negatively charged GNPs prepared by standard Turkevich–Frens method were washed from any residual salt remaining in solution after the synthesis and injected simultaneously with methanol and a small amount of NaCl. An immediate color change from deep red to purple was observed, indicating the initiation of aggregation process. Indeed, as methanol is less polar than water, it provides a thinner electrical double layer around nanoparticles which, due to reduction of the electrostatic repulsive force between nanoparticles, become less stable against the increase of the ionic strength induced by NaCl. To preserve a specific size and organization as well as to provide a favorable steric stabilization, we coated the formed nanoaggregates with Pluronic F127 polymer.

The formation of nanoaggregates was first ascertained by UV–vis–NIR extinction measurements (Figure 2A). Relative to nonaggregated GNPs which exhibit the well-known localized surface plasmon resonance (LSPR) band located at 520 nm of full-width-at-half-maximum (fwhm) of 44 nm (spectrum a), the nanoaggregates stabilized by Pluronic (GNPA-F127) exhibit LSPR spectrum red-shifted to 556 nm and fwhm = 92 nm (spectrum b). Moreover, in the absence of stabilization (spectrum c) the aggregation process evolves toward precipitation after 1 day, in contrast to GNPA-F127 which remain stable for several months of storage.

The morphology and size of GNPA-F127 were analyzed by TEM measurements. The representative TEM picture in Figure 2B reveals 3D globular quasi-spherical arrangements with mean diameter of 54 ± 13 nm (Figure 2C) obtained by assembling individual GNP of mean diameter of 12 ± 1 nm (Supporting Information Figure S1). It is worth noting that the capping Pluronic layer is faintly visible as a shadow enclosing GNPA (see the zoomed inset in Figure 2B).

To further analyze the size and stability of GNPA-F127, DLS and zeta-potential measurements were performed. The DLS data (Table 1) give information about the mean hydrodynamic diameter of nanoparticles which is larger than that provided by TEM measurements. The mean hydrodynamic diameter of individual bare GNP is 17 nm relative to 12 nm given by TEM which reaches 36 nm after encapsulation in Pluronic (GNP-127) and 75 nm for the aggregate GNPs encapsulated in Pluronic (GNA-F127). Note as reference the mean hydrodynamic diameter of 23 nm of Pluronic micelles formed in solution at the polymer concentration above the critical micelle concentration. From TEM and DLS data, we can assume a Pluronic corona of about 8–10 nm. Pluronic is an amphiphilic block copolymer composed of a hydrophobic poly(propylene oxide) (PPO) block symmetrically enclosed by two hydrophilic poly(ethylene oxide) (PEO) blocks. It is known that Pluronic is able to adsorb onto the nanoparticles surface via the PPO block and stabilize the nanoparticles through hydrophilic interactions with water, providing long-term stability for colloidal dispersions of nanoparticles in water.[17] It is conceivable that the interaction of hydrophilic chains (PEO) from the polymer coating with negatively charged hydroxyl groups from water results in moderate negative zeta potential value for Pluronic micelles. Indeed, from our zeta-potential measurements it was observed that the high negative surface charge of GNPs prepared by standard Turkevich–Frens method decreased as a result of polymer coating. As the zeta potentials of GNP-F127 and Pluronic F127 micelles are close (−5 mV vs −2 mV) and the sizes of GNP and micelles are congruent (12 nm vs 23 nm), it is likely that a core–shell structure is formed by full inclusion of GNPs in micelles. However, the relative higher size of nanoaggregates (36 nm) exhibiting a rough surface partially neutralized by the aggregation agent could explain the value of negative zeta potential (−24 mV) in the case of GNPA-F127.

Table 1. DLS and Zeta-Potential Data

	GNP	F127 micelles	GNP-F127	GNPA-F127
hydrodynamic diameter (nm)	17	23	36	75
PDI[a]	0.24	0.3	0.4	0.22
zeta-potential (mV)	−44	−2	−5	−24
zeta-deviation (mV)	8	5	6	10

[a] PDI—polidispersity index.

As the above fabricated nanoaggregates are designed to carry MB photosensitizer into cells to operate as both spectroscopic tags and PDT agents, the evaluation of MB loading efficiency is an essential step in our work. The loading was realized by coincubation of colloidal solution with MB solution at a final concentration of 2×10^{-5} M, followed by a careful washing out of unbound molecules. The extinction spectra of MB-loaded nanoparticles (both GNP-F127-MB and GNPA-F127-MB) are presented in Figure 3 in comparison with the spectra of unloaded counterparts and the absorption spectrum of free MB solution as reference. The increase of the total absorbance in the 550–700 nm range relative to the unloaded nanoparticles is taken as first indicator of successful loading. A better visibility of spectral modification occurring in the case of GNP-F127 is explainable by the narrow LSPR band which avoids overlapping with the MB absorption spectrum, and also by the higher final

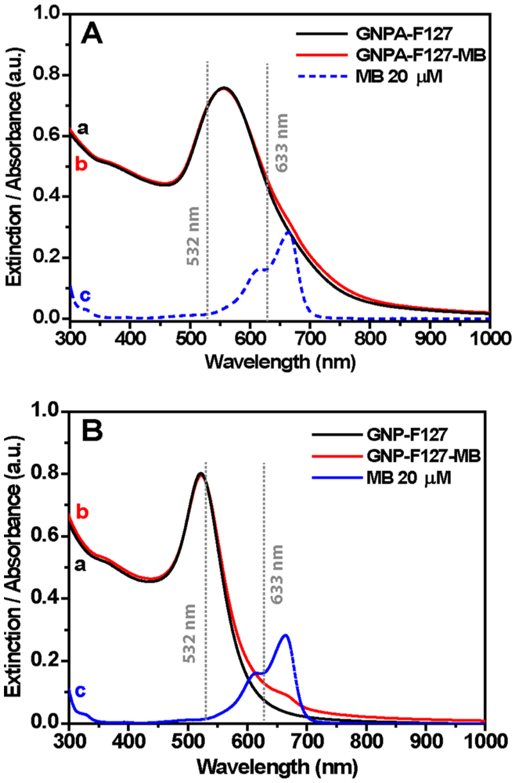

Figure 3. (A) UV−vis−NIR extinction spectra of GNPA-F127 (a) and GNPA-F127-MB (b) colloids and absorption spectrum of 2 × 10^{-5} M aqueous solution of MB (c); (B) UV−vis−NIR extinction spectra of GNP-F127 (a) and GNP-F127-MB (b) colloids and absorption spectrum of 2 × 10^{-5} M aqueous solution of MB (c). The dotted lines mark the positions of the two laser lines used in SERS measurements.

concentration of MB loaded (4 × 10^{-6} M relative to the 1.7 × 10^{-6} M in the case of aggregates).

SERS Characterization. A more specific characterization of the presence of MB in the composition of hybrid plasmonic nanoparticles can be provided by SERS analysis. Moreover, as the main mechanism in SERS is related to the excitation of surface plasmon resonance, the SERS measurements are indicative for the degree of aggregation and specific localization of MB molecules in nanoaggregates. Therefore, before using MB-loaded nanoaggregates as SERS-active tags in cell, we performed a careful SERS characterization of MB-loaded nanoaggregates in aqueous solution with two laser excitation lines, namely 532 and 633 nm. Figure 4A shows SERS spectra recorded at 532 nm laser excitation from GNP-F127-MB and GNPA-F127-MB colloidal solutions. The overall SERS enhancement is rather modest in both cases, although the nanoaggregates GNPA-F127-MB are about three times more SERS active than the individual GNP-F127-MB due to enhanced local field in aggregates. Despite the good resonance between the laser line and the LSPR bands (see the laser line in Figure 3), the low SERS signal is related to the strong damping of plasmon excitation when using laser excitation line in the vicinity of electronic interband transitions of gold metal and possible SERS signal reabsorption.[18,19] In the case of using the laser line at 633 nm, which is in resonance with the electronic transition of MB but not with the LSPR band of nonaggregated GNP-F127-MB, only a broad fluorescence signal is recorded (Figure 4B). On the contrary, in the case of aggregates (GNPA-F127-MB) both the electronic transition of MB and partially the LSPR band of aggregates (GNPA-F127-MB) are in resonance with the laser line. As a result the SERS signal is strong enough and overcomes a certain fluorescence background which is quite similar to that recorded from GNP-F127-MB. However, the recording of SERS signal together with fluorescence is unusual but interesting and enlightens a dual-modal detection of the presence of MB in nanoaggregates. It is obvious that a direct contact between the molecule and metal surface is detrimental to fluorescence due to the nonradiative loss, while a noncontact attachment far from metal surface could be again unfavorable to SERS. Therefore, from the above results we infer the possibility that MB molecules are loaded in two distinct sites: (1) some amount of molecules are electrostatically or chemically attached to the negatively charged surface of the gold nanoparticles to provide SERS signal[20] while (2) another amount of molecules are caged into the polymeric shell isolated from the metal surface (see Figure 2B) to provide fluorescence signal. This hypothesis has been advanced in one of our previous studies and supported here by steady-state and time-resolve fluorescence measurements presented later in the text.[21] The origin of the intense SERS signal detected from nanoaggregates under excitation at 633 nm laser line deserves a special comment. Since the 633 nm laser line is in resonance with both the LSPR band and the electronic transition of fluorophore (see Figure 3), we are actually measuring surface-enhanced resonance Raman Scattering (SERRS) spectrum. It is known that the resonance Raman spectroscopy has greater sensitivity compared to its non-resonance counterpart as well that SERRS could provide higher enhancement as compared to the nonresonant SERS.[22] In fact, in addition to the electromagnetic enhancement, the electronic resonant excitation of MB greatly enhances the cross section of the molecule, and the vibrational bands attributed to the chromophore skeleton are selectively enhanced by the mechanism of chromophore−plasmon coupling. Indeed, we clearly notice that the skeletal C−N−C bending modes of MB manifest very intensely at 451 and 505 cm^{-1} when excited at 633 nm (spectrum a in Figure 4B) but remain almost

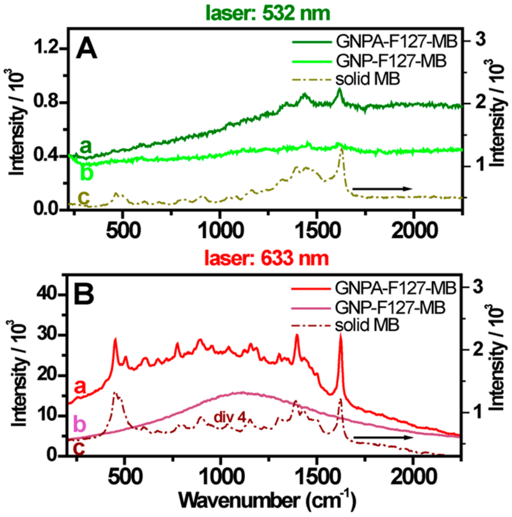

Figure 4. (A) SERS spectra of GNPA-F127-MB (a) and GNP-F127-MB (b) colloidal solutions and ordinary Raman spectrum of solid MB (c) at 532 nm excitation wavelength; (B) SERRS spectra of GNPA-F127-MB (a) and GNP-F127-MB (b) colloidal solutions and ordinary resonant Raman spectrum of solid MB (c) at 633 nm excitation wavelength.

unobserved when excited out of electronic resonance at 532 nm (spectrum a in Figure 4A). This is a clear evidence for SERRS. On the other hand, some intense bands in spectrum a in Figure 4B which are attributed to the C−C ring stretching (1627 cm^{-1}) and C−N symmetric stretching (1398 cm^{-1}) should be also enhanced via the electromagnetic mechanism as they are still visible in nanoaggregates excited out of electronic resonance at 532 nm. So, in the case of GNPA-F127-MB excited at 633 nm both the electromagnetic enhancement due to the plasmon resonance and the electronic enhancement due to molecular excitation are operative. The relative contribution of each enhancement mechanism in the SERRS signal is beyond the aim of this study. The above considerations about the higher intensity of Raman spectrum and in particular of vibrational bands coupled with MB chromophore hold also when comparing the ordinary resonant Raman spectrum (spectrum c in Figure 4B, divided by 4) with its nonresonant counterpart (spectrum c in Figure 4A). Finally, the GNPA-F127-MB nanoaggregates endowed with strong SERRS signal from MB molecules localized in so-called "hot-spots" are promising for further investigation as spectroscopic labels in cell imaging.

Fluorescence Lifetime Characterization. As stated before, MB-loaded nanoaggregates carry also a fluorescence signal, and time-resolved fluorescence measurements are necessary for further characterization. The fluorescence lifetime is extremely sensitive to the close molecular environment encountered by photosensitizer in both aqueous solution and cellular compartments. Any modification of fluorescence lifetime induced by interaction with plasmonic nanoparticle, polymer coating, or cytosol has direct impact on the rate of intersystem crossing which finally dictates the efficiency of photodynamic reaction. In the following, we determined the fluorescence lifetime of MB in four different environments: free MB in water, MB complexed to Pluronic F127 micelles in water, and loaded to GNP-F127 and GNPA-F127 nanoparticles in colloidal suspensions. The recorded fluorescence decay profiles are presented in Figure 5 together with exponential decay curves used for fitting the experimental data. The fluorescence lifetime values are summarized in Table 2.

Aqueous solution of free MB (10^{-6} M) exhibits single-exponential fluorescence decay with an average lifetime of 400 ps. Both complexation with Pluronic and loading to GNP-F127 and GNPA-F127 nanoparticles induce double-exponential behavior and increase of the average lifetime of MB (see Table 2). In concordance with our previous results,[20] these findings can be ascribed to the decreased polarity and increased viscosity of the microenvironment of MB molecules residing in the hydrophobic PPO chains and hydrophilic PEO chains of Pluronic, respectively. Compared to the lifetime values obtained in the case of the MB−Pluronic complex, GNP-F127-MB and GNPA-F127-MB show a slight increase of the shorter lifetime component; however, the larger component experienced a small decrease. This shortening of the larger component is plausible due to the increase of the radiative rate which is frequently experienced when fluorophores are placed in the close proximity of metallic surfaces and the fluorophore−plasmon coupling effect takes place. However, the overall lifetime increases upon loading, which consequently increases the probability of the intersystem crossing and provides considerable advantages regarding the imaging and photodynamic properties of our nanoparticles.

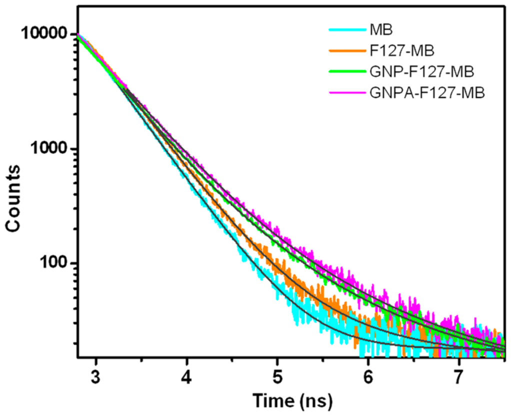

Figure 5. Time resolved fluorescence decay curves of aqueous solution of free MB, Pluronic F127-MB complex, and colloidal solutions of GNP-F127-MB and GNPA-F127-MB.

3.2. Multimodal Microscopy and Imaging of C-26 Cells with MB-Loaded Gold Nanoaggregates.

DF and DIC Microscopy. The internalization of nanoparticles by C-26 cells and their distribution inside cells were first evaluated by dark field and DIC microscopy. Gold nanoparticles are known to strongly scatter visible light at wavelengths of their localized plasmon resonance; therefore, they can be easily visualized and differentiated using DF microscopy, a widely used microscopic technique in imaging of biological cells.[23] It is well-known that the optical absorption and scattering are largely dependent on the size of the gold nanoparticles. For instance, in the case of spherical gold nanoparticles smaller than 20 nm, the total extinction is nearly all originating from absorption, whereas for nanoparticles of 80 nm, the absorption and scattering processes contribute in a comparable degree.[24] Both assembly and deviations of nanoparticles shapes from isotropic forms also increase the scattering contribution to the total extinction, making these nanoparticles more adequate for DF imaging.[25] Compared to the control C-26 cells (without gold nanoparticles), which show a very weak intrinsic scattering (Figure 6A), those incubated with GNP-F127-MB present a few green to yellow spots in the perinuclear region (Figure 6B). As GNP-F127-MB are too small to scatter intensely the incoming light, this scattering arises from the nanoparticles agglomerated in cellular compartments. Unlike GNP-F127-MB, GNPA-F127-MB present strong scattering and can be observed as clearly visible orange-red spots throughout all the cytoplasmatic region of the cell within internal vesicles such as endosomes and lysosomes (Figure 6C). It is worth mentioning that no nanoparticle internalization into the nuclei was observed which is plausible as the size of GNPA-F127-MB does not permit to cross the nuclear membrane via the nuclear pores, and neither specific nucleus targeting agent was used.

As DF microscopy does not permit to analyze in detail the distribution of nanoparticles along the cells' depth, we performed DIC imaging of the same cells for more precise information on localization and distribution. DIC microscopy relies on the contrast created by the refractive index gradients of different areas of a specimen and permits optical sectioning of thick specimens such as cells. Therefore, this technique enables imaging of a single focal plane of a cell which can be extremely useful in investigating the uptake and distribution of nanoparticles. In our case the nanoparticle distribution was assessed by imaging the same cell by focalizing at different

Table 2. Fluorescence Decay Parameters of MB, F127-MB, GNP-F127-MB, and GNPA-F127-MB Solutions[a]

	τ_1 (ps)	A_1 (%)	τ_2 (ps)	A_2 (%)	τ_a (ps)	χ^2
MB	400 ± 1	100	–	–	400	1.038
F127-MB	406 ± 2	96.9 ± 0.4	1125 ± 50	3.1 ± 0.4	465 ± 1	0.976
GNP-F127-MB	431 ± 3	87.3 ± 0.7	1018 ± 20	12.7 ± 0.6	582 ± 1.6	1.055
GNPA-F127-MB	432 ± 5	83.1 ± 1.4	985 ± 30	16.9 ± 1.4	607 ± 2	1.007

[a] τ_1, τ_2—fluorescence lifetimes; A_1, A_2—percent distribution of the different components; $\tau_a = (\sum \alpha_i \tau_i^2)/(\sum \alpha_i \tau_i)$; χ^2statistical parameter indicating quality of the exponential fit.

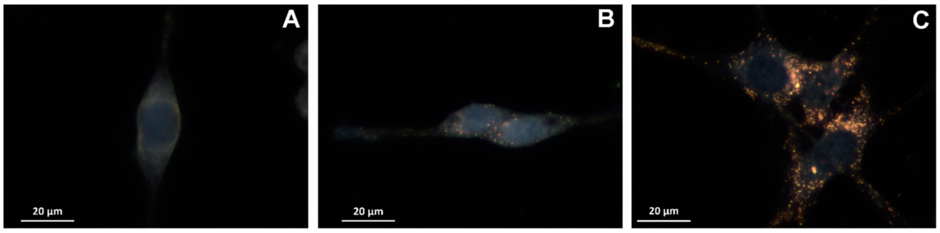

Figure 6. DF scattering images of control C-26 cells (A) and C-26 cells incubated for 20 h with GNP-F127-MB (B) and GNPA-F127-MB (C).

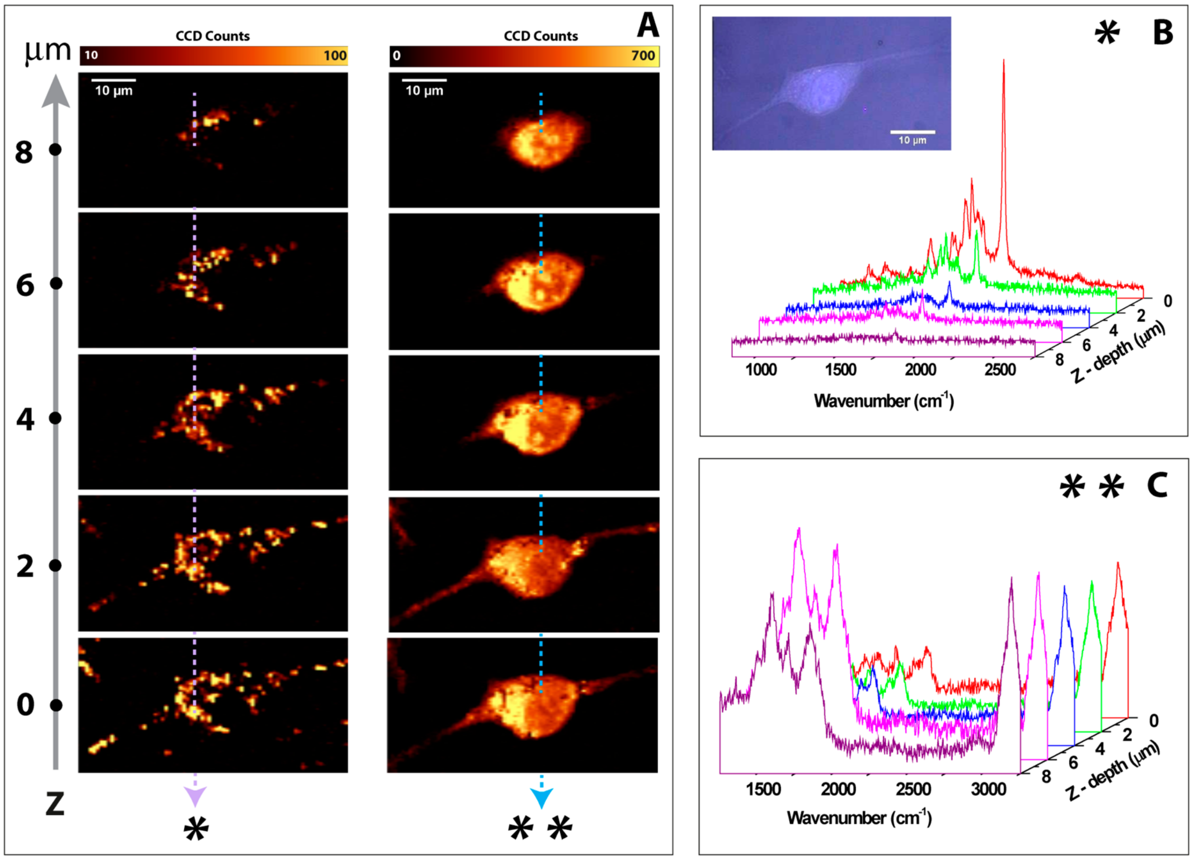

Figure 7. (A) SER(R)S maps of C-26 cells incubated with GNPA-F127-MB generated by plotting the intensity of a characteristic Raman peak over the scanned area. The nanoparticle localization (left column) was obtained at excitation with the laser line at 633 nm using the peak centered at 1623 cm^{-1} (C–C ring stretching vibrations of MB). The basic cellular structure (right column) was visualized at excitation with the laser line at 532 nm using the peak at 2800–3100 cm^{-1} C–H stretching vibrations of lipids). (B) Correspondent extracted SERRS spectra from each Z at the spot marked with the arrow and * in (A). The inset shows the bright field image of the scanned cell. (C) Correspondent extracted SERS spectra from each Z at the spot marked with the arrow and ** in (A).

planes of the cell in the Z direction starting from the surface of the Ibidi dish (considered as $Z = 0$ μm) and recording images from 2 to 2 μm until reaching the cell membrane (Supporting Information Figure S2). Likewise in DF scattering images, DIC images reveal extranuclear localization of the nanoparticles, which can be visualized in the whole cytoplasmic region at the entire height of the cells. It is noteworthy that no nanoparticles were found bound at the cell membrane, which also confirms their successful internalization inside cells.

Raman and SERRS Imaging. As the uptake of GNPA-F127-MB by C-26 cells was clearly demonstrated by DF and DIC microscopy, in the next step we examined if our nanoparticles

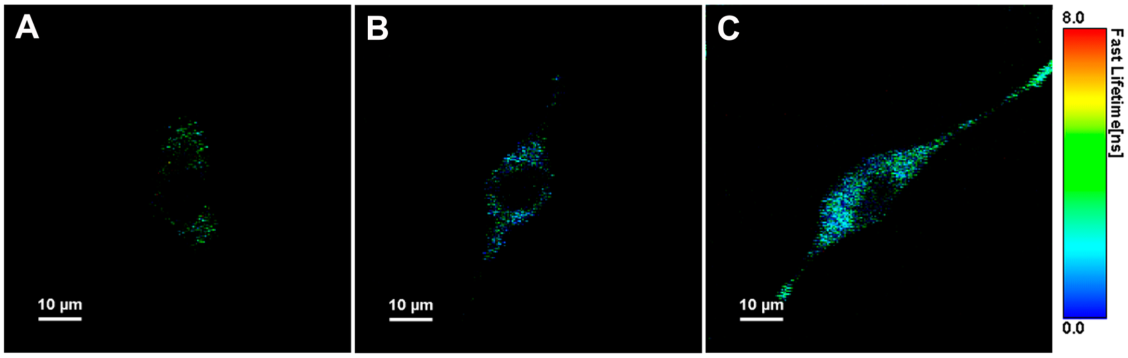

Figure 8. FLIM image of control C-26 cell (A), C-26 incubated with GNPA-F127-MB (B), and GNP-F127-MB (C) at 640 nm laser excitation.

can be used as reliable SERRS contrast agents for cellular imaging. In order to map out the nanoparticle distribution inside the cells, the 633 nm laser line was used for excitation, and *XY*-plane slices of a selected cell were imaged at different *z*-depths. The same *Z* slices of the same cell were also scanned using the 532 nm laser line for excitation which permits to entirely visualize the cell and to identify specific cellular components. Due to the efficient amplification of the Raman signal of the embedded MB molecules which is also well preserved inside cells, using the 633 nm excitation we can afford to use a relatively low laser power (1.1 mW) and an integration time of 0.1 s which resulted in a scanning time of ∼10 min per slice. In the case of the 532 nm laser line, a significantly larger laser power (14 mW) was used with an integration time of 0.3 s in order to obtain an adequate Raman signal of cells. In these conditions, five different cell slices were imaged at steps of 2 μm, starting from the cell−glass interface (indicated by the few uninternalized nanoparticles that remained attached to the glass surface) considered as $Z = 0$ μm.

Two-dimensional spectral maps for each *Z*-scan were generated (Figure 7A). The basic cellular structure was visualized using the peak at 2800−3100 cm^{-1} originating from the C−H stretching vibrations of lipids (right column in Figure 7A), while the nanoparticle localization was obtained by integrating the intensity of the characteristic band of MB centered at 1623 cm^{-1} attributed to the C−C ring stretching vibrations (left column in Figure 7A). The obtained SERRS maps representing the intracellular distribution of the nanoparticles are in good concordance with both the DF and DIC images. Although a few uninternalized nanoparticles could be detected at the substrate at the $Z = 0$ μm slice, SERRS maps clearly demonstrate a robust cellular uptake of GNPA-F127-MB nanoparticles which can be accurately detected at a 3D level inside cells. Nanoparticles are distributed throughout the cytoplasmic region making it possible to visualize and reconstruct the whole cell starting from their conjunction to the cultivation substrate via the actin filaments up to plasma membrane which physically separates the intracellular components from the extracellular environment. Similarly to the DF and DIC images, the nucleus of the cells is clearly delimitated as a black circle (no SERS signal from nanoparticles), indicating a strict extranuclear localization of the nanoparticles. In order to observe the variations of the SERRS signal of GNPA-F127-MB nanoparticles at different *Z*-depths, in Figure 7B and Figure 7C we show the SERS spectra obtained at each *Z* slice extracted from two different representative points (marked with pink and blue arrows) from the two series of spectral maps obtained at 633 and 532 nm laser excitation, respectively. In the first case, the most striking differences between spectra recorded at different *Z*-depth are obviously attributed to the intensity of the SERRS signal which repeatedly demonstrates the 3D distribution of the nanoparticles. However, by analyzing the presented spectra, discrete but evident variations of the SERRS signal from one spectrum to another can be observed. For instance, relative shifts of the peak maxima and some additional bands compared to the SERRS spectrum of the GNPA-F127-MB nanoparticles measured in the colloidal solution can be observed (the most prominent differences are marked with a dotted line in Figure S3A in the Supporting Information) which might be attributed to the amplified Raman signals from biological molecules which are adsorbed onto the surface or came into contact with the nanoaggregates. This observation is in good concordance both with the Raman maps obtained at 532 nm excitation and with the extracted spectra presented in Figure 7C which indicate amplified Raman signal of cellular components at the locations where nanoaggregates are present. In order to investigate in detail if our nanoparticles are certainly able to amplify the Raman signal of the cellular structure, gold nanoaggregates stabilized with Pluronic but without MB (GNPA-F127) were incubated to cells using the same incubation parameters (nanoparticle concentration, incubation time) as in the case of GNPA-F127-MB. Some spectra recorded randomly from inside the cells at 633 nm laser excitation are presented in Figure S3B in the Supporting Information. Indeed, GNPA-F127 are able to amplify the Raman signal of the cellular components, but the SERS spectra present high fluctuations. The most prominent bands, such as 991, 1142, and 1283 cm^{-1}, originate from the stretching vibrations of proteins,[26] while 1430 and 1510 cm^{-1} are attributed to the adenine and guanine nucleobases.

It is known that gold nanoparticles easily aggregate in cellular environment, which is widely exploited in SERS imaging and detection applications.[27] However, this aggregation process can hardly be controlled, which can result in undesired effects. In order to emphasize the pertinence of the controlled aggregation and stabilization of the nanoparticles for intracellular SERRS imaging application, control experiments were performed using individual spherical nanoparticles with the same surface chemistry (stabilized with Pluronic and loaded with MB, GNP-F127-MB). Both the incubation parameters of nanoparticles, both the imaging parameters were identical to those used in the case of GNPA-F127-MB. The obtained spectral maps (using the peak of MB centered at 1623 cm^{-1} for representation) are presented in Figure S4 in the Supporting Information. SERRS maps corroborate well with DF images presented in Figure 6B, providing signal only in a few zones where spherical nanoparticles are agglomerated. The intensities of the spectral bands are also visibly lower compared to those obtained from GNPA-F127-MB, and only a few bands of MB can be identified. Based on these experiments we consider that GNPA-F127-MB are reliable contrast agents for intracellular applications.

Fluorescence Lifetime Imaging (FLIM). It is well-known that MB is easily reduced under biological conditions by enzymes to its nonfluorescent leuco-form, also losing its photosensitizing characteristics.[28] In a previous work we have demonstrated that the Pluronic shell of gold nanoparticles can protect the embedded MB molecules against enzymatic degradation.[20] Based on these results and taking also in consideration the increased lifetime of MB upon loading, demonstrated in the section 3.1, we expect that GNP-F127-MB and GNPA-F127-MB internalized in C-26 cells could also be detected by time-resolved fluorescence microscopy. FLIM measurements were performed on control C-26 cells and cells incubated with GNP-F127-MB and GNPA-F127-MB, respectively. Figure 8A presents the FLIM image of the control cells, showing a slight autofluorescence with average lifetime of 1780 ± 30 ps. The intensity averaged lifetimes of cells incubated with GNP-F127-MB and GNPA-F127-MB decreased relative to the control cell (as it can be also deduced from the color change of the FLIM images from Figure 8B and 8C) to 1530 ± 4 ps and 1400 ± 8 ps, respectively. This is not surprising as fluorescence emission of GNP-F127-MB (τ_{av} = 582 ± 1.6 ps in solution) and GNPA-F127-MB (τ_{av} = 607 ± 2 ps in solution) has significant contribution to the overall fluorescence decay of the cells.

3.3. PDT Performance of MB-Loaded Gold Nanoaggregates on C-26 Cancer Cells.

Singlet Oxygen Generation by MB-Loaded Gold Nanoaggregates in Solution. The application of GNPA-F127-MB as photosensitizing agents is related to their efficiency in singlet oxygen generation ($^1O_2$). The efficiency of singlet oxygen $^1O_2$ generation was evaluated using the chemical sensor DPBF as described in the Experimental section. First, the irradiation of free DPBF at 660 nm did not induce significant spectral modification of the quencher molecule (a decrease of ~5% is in the range of experimental errors, curve a from Figure 9). Irradiation of nonloaded GNPA-F127 (without MB) did not produce any $^1O_2$ either (curve b from Figure 9). However, irradiation of free MB in solution induced a significant decrease in DPBF absorption, losing ~95% from the absorption after 150 s of irradiation (curve c from Figure 9). Remarkably, the same degradation of the quencher was obtained after irradiation for only 40 s in the case of GNPA-F127-MB, indicating a much higher rate of $^1O_2$ generation (curve d from Figure 9).

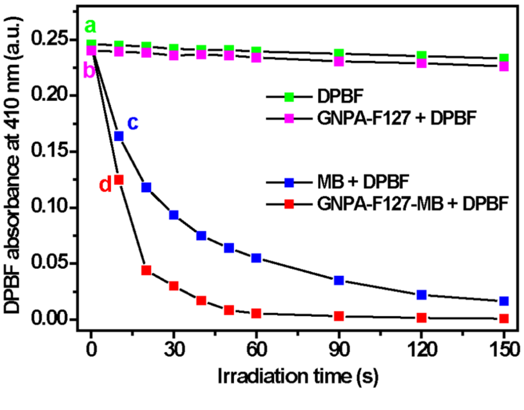

Figure 9. Time trace of DPBF absorbance intensity at 410 nm following irradiation at 660 nm of DPBF alone (a), DPBF mixture with GNPA-F127 (b), with MB free at concentration of 1.7×10^{-6} M (c), and DPBF mixture with GNPA-F127-MB (d). All samples were in ethanol, and the concentration of DPBF in all cases was of 8×10^{-5} M.

Dark Cytotoxicity of MB-Loaded Gold Nanoaggregates. Low dark toxicity is one of the major criteria when developing new photosensitizing agents, since the main side effects in clinical PDT result from the dark toxicity of photosensitizer to normal tissue.[29] Therefore, before performing PDT experiments, we evaluated the dark cytotoxicity of fabricated nanoparticles on murine colon carcinoma cancer cell line (C-26) for a concentration range of 20−120 μg/mL corresponding to the concentrations used in imaging assays and PDT experiments. Figure 10 shows the cell viability (measured as percentage of untreated cells) against different concentrations of MB-loaded GNPA-F127 and GNPA-F127, respectively. WST-1 assay indicates no significant dark toxicity in comparison with untreated cells, even for high dosage of nanoparticles (120 μg/mL) which qualify MB-loaded nanoaggregates for PDT experiments.

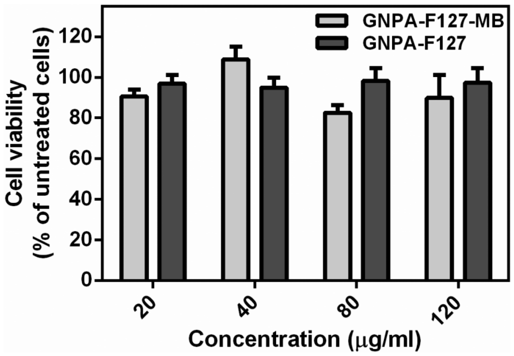

Figure 10. Cell viability of C-26 cells at increasing nanoparticle concentration.

PDT Performance of MB-Loaded Gold Nanoaggregates. The in vitro phototoxicity was evaluated by the direct observation of fluorescence images of cells stained with PI after irradiation under microscope. The cells were incubated with both free photosensitizer and GNPA-F127-MB at equimolar MB concentrations (1.7×10^{-6} M). Two control experiments were carried out on untreated cells and cells treated with blank GNPA-F127 (not MB loaded). After 24 h of incubation, cells were carefully washed with PBS and replaced with fresh culture medium. During the PDT assay, the cells were maintained in the microincubator mounted on the microscope stage, and the photoactivation was performed with 660 nm light from a LED source. In all cases a spot of about 600 μm was irradiated at 50 mW irradiation power (17.7 W/cm^2 power density) for 40 min. Fluorescence staining of the dead cells with PI was performed 4 h after irradiation. The viability of untreated cells was almost 100% after irradiation for 40 min (Figure 11 a-A), suggesting that this dose of irradiation power is safe for C-26 cells. Similarly, control nanoparticles GNPA-F127 (without MB) do not show any important phototoxicity to tumor cells (Figure 11b-B). Unexpectedly, free MB did not induce considerable cell destruction after irradiation at the concentration used in this study (Figure 11c-C). On the contrary, GNPA-F127-MB treated cells showed a

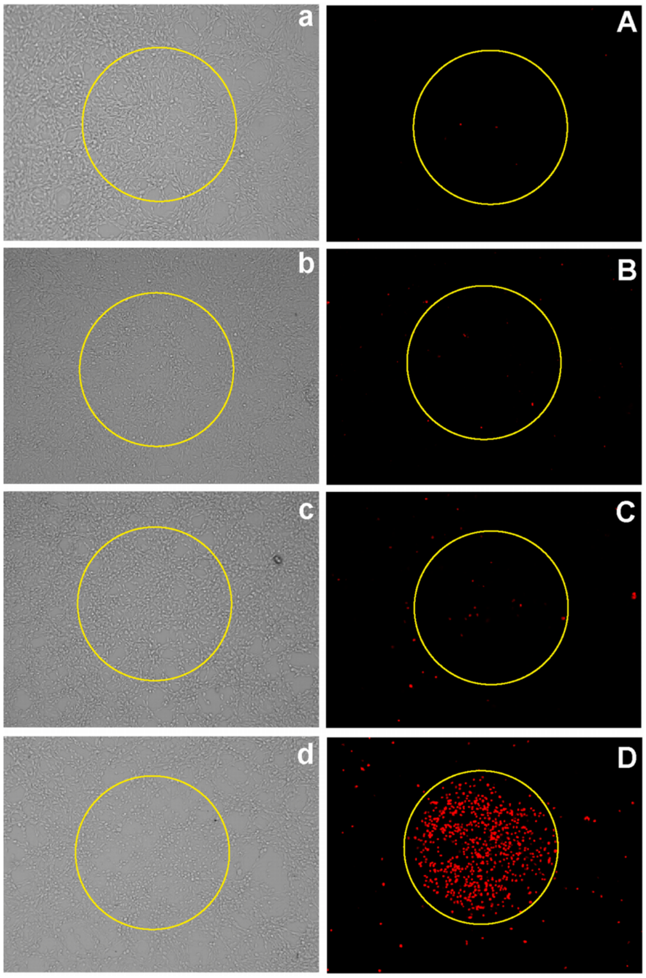

Figure 11. Transmitted light and immunofluorescent staining images of C-26 cell: not treated and irradiated (a, A), treated with GNPA-F127 and irradiated (b, B), treated with MB and irradiated (c, C), and treated with GNPA-F127-MB and irradiated. Irradiation performed by LED emitting at 660 nm for 40 min with a power of 50 mW (17.7 W/cm^2). The yellow circles represent the irradiated areas.

pronounced phototoxicity causing complete cell mortality in the irradiated area, indicating clearly a more efficient PDT effect (Figure 11d-D). This high difference in the in vitro photodynamic activity of photosensitizer in free MB state and conjugate to nanoaggregates (GNPA-F127-MB) can be explained by two effects. In the case of nonencapsulated MB, the low phototoxic effect could be mainly attributed to the enzymatic reduction of the free MB to its in color leuco form, which has no considerable PDT activity.[30] We recently demonstrated that Pluronic is able to protect MB from this enzymatic reduction,[20] a fact that could contribute to higher phototoxic effect of GNPA-F127-MB compared to the free MB. The second effect is attributed to the intrinsic plasmonic properties of GNPA-F127-MB nanoaggregates which are able to enhance the singlet oxygen generation, as we demonstrated above by using the chemical sensor DPBF in solution. As recently shown in literature, the enhanced electromagnetic field of plasmonic nanoparticles can promote the generation of $^1O_2$ with the presence of photosensitizer under light irradiation.[13,31] Hayden et al. systematically investigated the role of the overlap between the energy of the plasmon band and the absorption and emission of the photosensitizer protoporphyrin IX,[12] using different linkers to modulate the photosensitizer−particle distance. They found that the strongest enhancement of photosensitizer activity occurs in the case when the absorption of the photosensitizer overlaps with the plasmon band of the nanoparticles and when the drug is covalently bound close to the silver spherical nanoparticle surface. These considerations are valid also for our PDT experiments as the absorption of MB overlaps well with the plasmonic band of GNPA (see Figure 3) and the enhanced electromagnetic in GNPA-F127-MB is clearly proved by the SERS signal of MB (Figure 4). Furthermore, as stated before, the slight increase of fluorescence lifetime of MB upon conjugation could also contribute to the enhancement of $^1O_2$ generation by promoting the probability of the intersystem crossing.

4. CONCLUSIONS

In this work we proposed a new class of biocompatible nanoparticles based on Pluronic stabilized gold nanoaggregates of controlled size labeled with MB (GNPA-F127-MB) and demonstrated their applicability as multimodal contrast agents and highly efficient photodynamic agents of cancer cells. Specifically, we showed that GNPA-F127-MB can be visualized inside cells by DF and DIC microscopy, which proved to be useful techniques to evaluate the uptake of nanoparticles. Thereafter, we demonstrated that our nanoparticles provide a strong, distinct SERRS signal inside C-26 cancer cells that can be accurately detected at a 3D level inside cells. The efficient SERS amplification can be attributed to the MB molecules entrapped in the "hot spots" created between interconnecting nanoparticles. At the same time we showed that MB molecules separated from the metal surface by the polymer spacer can provide fluorescence signal allowing the detection of GNPA-F127-MB inside cells via FLIM. Furthermore, photodynamic studies confirmed that the conjugation of a MB to GNPA-F127 improves PDT efficiency compared to the free photosensitizer, without showing significant dark toxicity. This amplified photodynamic activity can be attributed to the enhanced singlet oxygen generation ability and improved photophysical properties of the GNPA-F127-MB complex.

Considering the enhanced optical and photodynamic activity of molecules in the presence of plasmonic nanoparticles, the approach implemented in the present study by combining SERRS active gold nanoparticles with molecules which exhibit both fluorescent and enhanced photodynamic properties represent a valuable tool in developing novel multifunctional nanoplatforms for nanomedicine with improved efficiency in diagnosis and therapy.

■ ASSOCIATED CONTENT

Ⓢ Supporting Information

TEM image of GNP, GNPA-F127, DIC microscopy images, several examples of SERS spectra collected from the cell, and some useful data derived from secondary experiments on nonaggregated gold nanoparticles. The Supporting Information is available free of charge on the ACS Publications website at DOI: 10.1021/acsami.5b04734.

■ AUTHOR INFORMATION

Corresponding Author

*E-mail: simion.astilean@phys.ubbcluj.ro. Phone: 0040-264-405300/0040-744628364.

Author Contributions

All authors have given approval to the final version of the manuscript.

Notes

The authors declare no competing financial interest.

■ ACKNOWLEDGMENTS

This work was performed with the financial support from Babes-Bolyai University, project number GTC_34015/2013. T.S. also acknowledges the financial support of the Sectorial Operational Program for Human Resources Development 2007-2013, cofinanced by the European Social Fund, under the project number POSDRU/159/1.5/S/132400. Authors acknowledge Adriana Vulpoi for the TEM measurements.

■ REFERENCES

(1) Fernandez-Fernandez, A.; Manchanda, R.; McGoron, A. J. Theranostic Applications of Nanomaterials in Cancer: Drug Delivery, Image-Guided Therapy, and Multifunctional Platforms. *Appl. Biochem. Biotechnol.* **2011**, *165*, 1628−1651.

(2) Singh, A.; Sahoo, S. K. Magnetic Nanoparticles: A Novel Platform for Cancer Theranostics. *Drug Discovery Today* **2014**, *19*, 474−481.

(3) Yang, K.; Feng, L.; Shi, X.; Liu, Z. Nano-graphene in Biomedicine: Theranostic Applications. *Chem. Soc. Rev.* **2013**, *42*, 530−547.

(4) Khlebtsov, N.; Bogatyrev, V.; Dykman, L.; Khlebtsov, B.; Staroverov, S.; Shirokov, A.; Matora, L.; Khanadeev, V.; Pylaev, T.; Tsyganova, N.; et al. Analytical and Theranostic Applications of Gold Nanoparticles and Multifunctional Nanocomposites. *Theranostics* **2013**, *3*, 167−180.

(5) Kuo, W.-S.; Chang, Y.-T.; Cho, K.-C.; Chiu, K.-C.; Lien, C.-H.; Yeh, C.-S.; Chen, S.-J. Gold Nanomaterials Conjugated with Indocyanine Green for Dual-Modality Photodynamic and Photothermal Therapy. *Biomaterials* **2012**, *33*, 3270−3278.

(6) Kuo, W.-S.; Chang, C.-N.; Chang, Y.-T.; Yang, M.-H.; Chien, Y.-H.; Chen, S.-J.; Yeh, C.-S. Gold Nanorods in Photodynamic Therapy, as Hyperthermia Agents, and in Near-infrared Optical Imaging. *Angew. Chem., Int. Ed.* **2010**, *49*, 2711−2715.

(7) Chen, W.-H.; Xu, X.-D.; Jia, H.-Z.; Lei, Q.; Luo, G.-F.; Cheng, S.-X.; Zhuo, R.-X.; Zhang, X.-Z. Therapeutic Nanomedicine Based on Dual-Intelligent Functionalized Gold Nanoparticles for Cancer Imaging and Therapy in Vivo. *Biomaterials* **2013**, *34*, 8798−8807.

(8) Lombardi, J. R.; Birke, R. L. A Unified View of Surface-Enhanced Raman Scattering. *Acc. Chem. Res.* **2009**, *42*, 734−742.

(9) Aslan, K.; Gryczynski, I.; Malicka, J.; Matveeva, E.; Lakowicz, J. R.; Geddes, C. D. Metal-enhanced Fluorescence: An Emerging Tool in Biotechnology. *Curr. Opin. Biotechnol.* **2005**, *16*, 55−62.

(10) Zhang, Y.; Aslan, K.; Previte, M. J. R.; Geddes, C. D. Metal-Enhanced Singlet Oxygen Generation: A Consequence of Plasmon Enhanced Triplet Yields. *J. Fluoresc.* **2007**, *17*, 345−349.

(11) Khaing Oo, M. K.; Yang, Y.; Hu, Y.; Gomez, M.; Du, H.; Wang, H. Gold Nanoparticle-Enhanced and Size-Dependent Generation of Reactive Oxygen Species from Protoporphyrin IX. *ACS Nano* **2012**, *6*, 1939−1947.

(12) Hayden, S. C.; Austin, L. A.; Near, R. D.; Ozturk, R.; El-Sayed, M. A. Plasmonic Enhancement of Photodynamic Cancer Therapy. *J. Photochem. Photobiol., A* **2013**, *269*, 34−41.

(13) Terentyuk, G.; Panfilova, E.; Khanadeev, V.; Chumakov, D.; Genina, E.; Bashkatov, A.; Tuchin, V.; Bucharskaya, A.; Maslyakova, G.; Khlebtsov, N.; et al. Gold Nanorods with a Hematoporphyrin-Loaded Silica Shell for Dual-Modality Photodynamic and Photothermal Treatment of Tumors in Vivo. *Nano Res.* **2014**, *7*, 325−337.

(14) Khlebtsov, N.; Dykman, L. Biodistribution and Toxicity of Engineered Gold Nanoparticles: A Review of in Vitro and in Vivo Studies. *Chem. Soc. Rev.* **2011**, *40*, 1647−1671.

(15) Maher, R. C. SERS Hot Spots. In *Raman Spectroscopy for Nanomaterials Characterization*; Kumar, C. S. S. R., Ed.; Springer: Berlin, Heidelberg, 2012; pp 215−260.

(16) Frens, G. Controlled Nucleation for the Regulation of the Particle Size in Monodisperse Gold Suspensions. *Nature, Phys. Sci.* **1973**, *241*, 20−22.

(17) Rahme, K.; Gauffre, F.; Marty, J.-D.; Payré, B.; Mingotaud, C. A Systematic Study of the Stabilization in Water of Gold Nanoparticles by Poly(ethylene oxide)−Poly(propylene oxide)−Poly(ethylene oxide) Triblock Copolymers. *J. Phys. Chem. C* **2007**, *111*, 7273−7279.

(18) Rycenga, M.; Hou, K. K.; Cobley, C. M.; Schwartz, A. G.; Camargo, P. H. C.; Xia, Y. Probing the Surface-enhanced Raman Scattering Properties of Au−Ag Nanocages at Two Different Excitation Wavelengths. *Phys. Chem. Chem. Phys.* **2009**, *11*, 5903−5908.

(19) Sivapalan, S. T.; Devetter, B. M.; Yang, T. K.; van Dijk, T.; Schulmerich, M. V.; Carney, P. S.; Bhargava, R.; Murphy, C. J. Off-Resonance Surface-Enhanced Raman Spectroscopy from Gold Nanorod Suspensions as a Function of Aspect Ratio: Not What We Thought. *ACS Nano* **2013**, *7*, 2099−2105.

(20) Simon, T.; Boca-Farcau, S.; Gabudean, A.-M.; Baldeck, P.; Astilean, S. LED-activated Methylene Blue-loaded Pluronic-Nanogold Hybrids for in Vitro Photodynamic Therapy. *J. Biophotonics* **2013**, *6*, 950−959.

(21) Simon, T.; Boca, S. C.; Astilean, S. Pluronic-Nanogold Hybrids: Synthesis and Tagging with Photosensitizing Molecules. *Colloids Surf., B* **2012**, *97*, 77−83.

(22) McNay, G.; Eustace, D.; Smith, W. E.; Faulds, K.; Graham, D. Surface-Enhanced Raman Scattering (SERS) and Surface-Enhanced Resonance Raman Scattering (SERRS): A Review of Applications. *Appl. Spectrosc.* **2011**, *65*, 825−837.

(23) Orendorff, C. J.; Sau, T. K.; Murphy, C. J. Shape-Dependent Plasmon-Resonant Gold Nanoparticles. *Small* **2006**, *2*, 636−639.

(24) Jain, P. K.; Lee, K. S.; El-Sayed, I. H.; El-Sayed, M. A. Calculated Absorption and Scattering Properties of Gold Nanoparticles of Different Size, Shape, and Composition: Applications in Biological Imaging and Biomedicine. *J. Phys. Chem. B* **2006**, *110*, 7238−7248.

(25) Huang, X.; El-Sayed, M. A. Gold Nanoparticles: Optical Properties and Implementations in Cancer Diagnosis and Photothermal Therapy. *J. Adv. Res.* **2010**, *1*, 13−28.

(26) Kneipp, J.; Kneipp, H.; Wittig, B.; Kneipp, K. Novel Optical Nanosensors for Probing and Imaging Live Cells. *Nanomedicine* **2010**, *6*, 214−226.

(27) Kneipp, J.; Kneipp, H.; McLaughlin, M.; Brown, D.; Kneipp, K. In Vivo Molecular Probing of Cellular Compartments with Gold Nanoparticles and Nanoaggregates. *Nano Lett.* **2006**, *6*, 2225−2231.

(28) Gabrielli, D.; Belisle, E.; Severino, D.; Kowaltowski, A. J.; Baptista, M. S. Binding, Aggregation, and Photochemical Properties of Methylene Blue in Mitochondrial Suspensions. *Photochem. Photobiol.* **2004**, *79*, 227−232.

(29) Allison, R. R.; Downie, G. H.; Cuenca, R.; Hu, X.-H.; Childs, C. J.; Sibata, C. H. Photosensitizers in Clinical PDT. *Photodiagn. Photodyn. Ther.* **2004**, *1*, 27−42.

(30) Ogilby, P. R. Singlet Oxygen: There Is Indeed Something New under the Sun. *Chem. Soc. Rev.* **2010**, *39*, 3181−3209.

(31) Li, Y.; Wen, T.; Zhao, R.; Liu, X.; Ji, T.; Wang, H.; Shi, X.; Shi, J.; Wei, J.; Zhao, Y.; et al. Localized Electric Field of Plasmonic Nanoplatform Enhanced Photodynamic Tumor Therapy. *ACS Nano* **2014**, *8*, 11529−11542.